Heliyon

ELSEVIER

Received:
10 August 2015
Revised:
27 September 2015
Accepted:
30 September 2015

Heliyon (2015) e00036

Effect of aerosol vertical distribution on aerosol-radiation interaction: A theoretical prospect

Amit Kumar Mishra, Ilan Koren *, Yinon Rudich

Department of Earth and Planetary Sciences, Weizmann Institute of Science, Rehovot, Israel

* Corresponding author.

E-mail address: ilan.koren@weizmann.ac.il (I. Koren).

Abstract

This study presents a theoretical investigation of the effect of the aerosol vertical distribution on the aerosol radiative effect (ARE). Four aerosol composition models (dust, polluted dust, pollution and pure scattering aerosols) with varying aerosol vertical profiles are incorporated into a radiative transfer model. The simulations show interesting spectral dependence of the ARE on the aerosol layer height. ARE increases with the aerosol layer height in the ultraviolet (UV: 0.25–0.42 μm) and thermal-infrared (TH-IR: 4.0–20.0 μm) regions, whereas it decreases in the visible-near infrared (VIS-NIR: 0.42–4.0 μm) region. Changes in the ARE with aerosol layer height are associated with different dominant processes for each spectral region. The combination of molecular (Rayleigh) scattering and aerosol absorption is the key process in the UV region, whereas aerosol (Mie) scattering and atmospheric gaseous absorption are key players in the VIS-NIR region. The longwave emission fluxes are controlled by the environmental temperature at the aerosol layer level. ARE shows maximum sensitivity to the aerosol layer height in the TH-IR region, followed by the UV and VIS-NIR regions. These changes are significant even in relatively low aerosol loading cases (aerosol optical depth ~0.2–0.3). Dust aerosols are the most sensitive to altitude followed by polluted dust and pollution in all three different wavelength regions. Differences in the

http://dx.doi.org/10.1016/j.heliyon.2015.e00036

sensitivity of the aerosol type are explained by the relative strength of their spectral absorption/scattering properties. The role of surface reflectivity on the overall altitude dependency is shown to be important in the VIS-NIR and UV regions, whereas it is insensitive in the TH-IR region. Our results indicate that the vertical distribution of water vapor with respect to the aerosol layer is an important factor in the ARE estimations. Therefore, improved estimations of the water vapor profiles are needed for the further reduction in uncertainties associated with the ARE estimation.

Keywords: Atmospheric science, Atmospheric physics, Radiative transfer, Environmental science, Atmospheric aerosols, Atmospheric gases

1. Introduction

1.1. Motivation

Aerosols are a key component of Earth's radiative system. Aerosols can affect Earth's radiation budget in a direct way (aerosol-radiation interaction) by absorbing and scattering of solar/thermal radiation (Ghan et al., 2012; Leibensperger et al., 2012; Myhre et al., 2013a) and in indirect way (aerosol-cloud interaction) by modifying cloud microphysics and therefore hydrological processes (Altaratz et al., 2014; Baker and Peter, 2008; Boucher et al., 2013; Costantino and Bréon, 2013; Li et al., 2011; Stevens and Feingold, 2009). Therefore, aerosols are one of the most important forcing agents which largely contribute to the total uncertainties in estimated global climate radiative forcing (Boucher et al., 2013; Kahn, 2012; Leibensperger et al., 2012). Schwartz (2004) pointed out that in order to reduce and to bound the uncertainties in climate sensitivity, the uncertainties in aerosol forcing needed to reduce at least by three-fold. The uncertainties in aerosol forcing are mainly associated with limitations of accurate estimation of aerosol and cloud properties, their spatio-temporal variation (Kokhanovsky et al., 2010; Li et al., 2009), inadequate understanding of aerosol-cloud interaction processes (Rosenfeld, 2014; Tao et al., 2012), and relatively complex aerosol-cloud-climate feedback mechanisms (Boucher et al., 2013; Carslaw et al., 2010; Raes et al., 2010). Aerosol-radiation interaction effects have large uncertainties primarily associated with uncertainties in aerosol characterization, aerosol optical properties [e.g. aerosol optical depth (AOD), single scattering albedo (SSA), the asymmetry parameter (ASYM)] and their horizontal and vertical profiles (Boucher et al., 2013). The recent fifth assessment report (AR5) of the Intergovernmental Panel on Climate Change estimated the aerosol radiative effect to be –0.35 (–0.85 to +0.15) W m^{-2} at top of the atmosphere (TOA) for global-mean aerosol direct radiative forcing (Myhre et al., 2013b). The reported uncertainty estimates are based on a large

http://dx.doi.org/10.1016/j.heliyon.2015.e00036

set of observations and converging independent estimates of radiative forcing and differences between model estimates of radiative forcing.

Several initiatives have been taken to narrow down the uncertainties associated with aerosol properties through field experiments, closure studies, satellite observations, and data assimilation (Benedetti et al., 2009; Bergstrom et al., 2010; Bond et al., 2013; Christopher et al., 2009; Hansell et al., 2010; Kahn, 2012; Kleidman et al., 2012; Kulmala et al., 2011; Paredes-Miranda et al., 2009; Tanré et al., 2011; Zhang et al., 2012). Amidst all other uncertainties associated with aerosol properties, the inadequate information about the vertical distribution of aerosols (Heintzenberg et al., 2011) also greatly affects the aerosol radiative forcing estimation (Feng et al., 2015; Vuolo et al., 2014). Torres et al. (1998) reported the effect of absorbing aerosol with varying aerosol altitude layers on backscattered aerosol radiance in the near UV region. They have shown that the interaction between aerosols and the strong molecular scattering near the UV region produces spectral variations of the backscattered radiances that can be used to separate aerosol absorption from scattering effects. Liao and Seinfeld (1998) have shown that the clear-sky longwave (LW) forcing and cloudy-sky shortwave (SW) forcing at TOA are very sensitive to the altitude of the dust layer. The radiative effect of a biomass burning smoke layer could change their sign from negative (-13 W m^{-2}) to positive (11.5 W m^{-2}) in the presence of underlying stratus clouds (Keil and Haywood, 2003). The sensitivity of the aerosol forcing to the vertical distribution of aerosol depends on the presence of clouds, surface albedo and aerosol properties (Choi and Chung, 2014). Haywood and Shine (1997) and thereafter many other studies emphasized that the vertical distribution of aerosol (e.g. soot and sulphate) relative to the clouds must be established for accurate assessment of the radiative effect of anthropogenic aerosols (Chand et al., 2009; Graaf et al., 2012; Meyer et al., 2013; Peters et al., 2011; Wilcox, 2012; Zarzycki and Bond, 2010). Some of these studies also discuss implications of aerosol vertical distribution on the radiative heating/cooling associated with large-scale atmospheric dynamics. Most of the above mentioned studies cover either small portion of wavelength regions (Torres et al., 1998) or integrated results over the entire solar/thermal wavelength regions (Liao and Seinfeld, 1998), which make it difficult to understand all the responsible competitive physical processes.

This study uses four different aerosols models (dust, polluted dust, pollution and pure scattering aerosols) with twenty aerosol profiles incorporated in the Santa Barbara DISORT Atmospheric Radiative Transfer (SBDART) model in order to clarify the effect of the vertical distribution of the aerosol layer on the aerosol radiative effect (ARE). To follow the main processes and explain the synergism and competition between them, we divide the complete solar and thermal spectral region into three main bands: the ultraviolet (UV: 0.25–0.42 μm), the

http://dx.doi.org/10.1016/j.heliyon.2015.e00036

visible-near infrared (VIS-NIR: 0.42–4.0 μm) and the thermal-infrared (TH-IR: 4.0–20.0 μm) region, and analyze the governing effect and sensitivity to aerosol layer height, aerosol types and surface albedo per region.

1.2. Theoretical background

Fig. 1 shows schematically key radiative processes (upper panel) and atmospheric absorption spectrum (lower panel) in a cloud-free scenario. The two sources of radiation energy in the atmosphere are the solar radiation from the Sun and the emitted thermal radiation from the Earth's surface. There are several competitive processes in these regimes which account for the overall radiation budget. The solar radiation comprises ultraviolet (0.01–0.4 μm), visible (0.4–0.7 μm) and near-infrared (0.7–4.0 μm) radiation. Extremely short ultraviolet (0.01–0.1 μm) is screened out by nitrogen. Most of the ultraviolet radiation in 0.1–0.32 μm is screened by combination of O_2 (<0.2 μm) and stratospheric ozone (~0.2–0.32 μm) and only light in the range 0.32–0.4 μm significantly reaches the troposphere (Seinfeld and Pandis, 2012). The unmasked ultraviolet and most of the visible and near-infrared radiations reach the Earth's

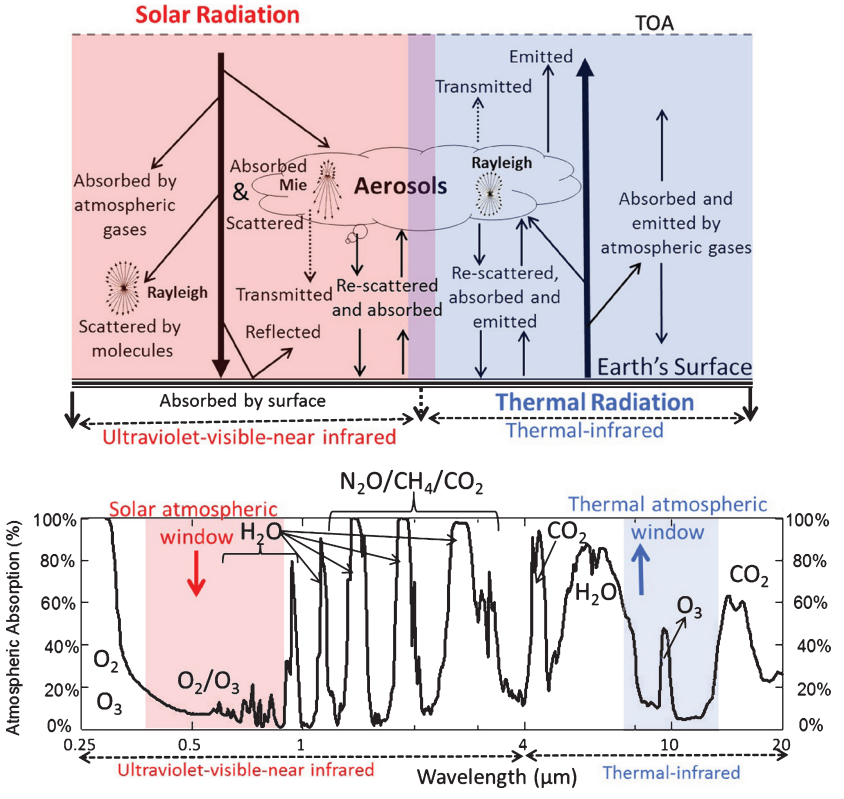

Fig. 1. Schematic illustrations of the key processes during radiation-atmosphere interaction in a cloud free scenario (upper panel) and atmospheric absorption spectrum (lower panel). Red and blue colors are used to highlight the solar and thermal region, respectively.

http://dx.doi.org/10.1016/j.heliyon.2015.e00036

troposphere where for the cloud free regimes it interacts with atmospheric gases, aerosols and Earth's surface.

The atmospheric gases and aerosols attenuate the solar radiation either by scattering or absorption. The scattering is a strong function of size of atmospheric constituents and wavelength of incident radiation. In general, the sizes of atmospheric constituents vary from few nm (gases) to few μm (aerosols). The scattering caused by the particles which are smaller in size than the wavelength of radiation is called Rayleigh scattering. Rayleigh scattering mainly consists of scattering from atmospheric gases (N_2 and O_2) in the solar region with maximum strength for ultraviolet to blue light. However, the scattering by aerosol particles in the atmospheric thermal window (~7–13 μm) could be also treated as Rayleigh scattering. The strength of Rayleigh scattering significantly decreases for higher wavelengths (λ) as λ^{-4} (van de Hulst, 1981). The Rayleigh phase function is nearly isotropic and symmetric with respect to the scattering angle $\theta = 90°$, i.e. asymmetry parameter (g) equal to zero. Aerosols can interact with the scattered radiation by molecules depending on their spectral properties. Mie scattering, that is, scattering by aerosol when the particle size is equivalent to the wavelength of radiation, dominates in the atmospheric solar window (~0.4–0.9 μm). In general, aerosol particles have $g > 0.5$ which indicate the dominance of forward scattering. Again the scattered radiation by aerosols can interact with other aerosol particles or by atmospheric gases and can be re-scattered or absorbed depending on their spectral properties. Water vapor, O_3, CO_2 and other atmospheric gaseous constituents (N_2O, CH_4 etc.) can also absorb the incoming radiation in solar region (Fig. 1, lower panel) either in broad or narrow absorption bands (Seinfeld and Pandis, 2012). However, the tropospheric gaseous absorptions play the dominant role only in the near infrared region as compared with the rest of the solar band. The transmitted radiation through the atmosphere reaches the underlying surface and may be absorbed or reflected, depending on the surface properties.

Aerosol layers (especially large size particles) also scatter and absorb the thermal infrared radiation coming from below and emit infrared radiation depending on their emissivity and temperature. These processes dominate in the thermal atmospheric window where the atmosphere is nearly transparent for atmospheric absorption (Fig. 1, lower panel). The scattered and emitted thermal radiation by aerosols could also re-scattered, absorbed and re-emitted again by other aerosol particles. Similar to the solar radiation, various greenhouse gases absorb the thermal-infrared radiation and re-emit it. The main absorbing gases in the thermal region are the water vapor, O_3 and CO_2 (Fig. 1, lower panel).

http://dx.doi.org/10.1016/j.heliyon.2015.e00036

2. Materials and methods

The layout of the methodology used in this study is shown in Fig. 2. The estimation of aerosol radiative effects strongly depends on the key input parameters e.g. aerosol optical and microphysical properties, aerosol vertical distribution, atmospheric gaseous profiles, meteorological variables, and surface properties incorporated in radiative transfer schemes. Aerosols show large spatial and temporal variability in optical and microphysical properties across the globe (Kinne et al., 2006). Their vertical and horizontal distribution strongly depends on the meteorological parameters that modulate their removal and transport processes. The optical and microphysical properties of the various aerosol types cover a wide range of values (Hess et al., 1998). A theoretical analysis using all aerosol types is a complicated and impractical approach. Therefore, to reduce the complexity, we have selected a set of aerosol models that represent the commonly observed aerosol types across the globe. The aerosol models including dust, polluted dust, and pollution used as inputs in the radiative simulations were synthesized using optical and microphysical properties observed from 24 AERONET stations (Fig. 3) around the Mediterranean Basin (Mishra et al., 2014). Each station is categorized as either dust affected or pollution dominated site depending on source region and known aerosol types. AERONET-derived size parameters (Extinction Angstrom Exponent (EAE)) are used for the classification of aerosol types viz. dust (EAE $<$ 0.6), polluted dust (0.7 $<$ EAE $<$ 1.1), and pollution (EAE $>$ 1.4). Since the AERONET-derived aerosol optical properties are only available in the 0.4–1.0 μm wavelength range, observed particle size distributions and refractive indices are used to extrapolate the aerosol optical properties in the entire wavelength region (0.25–20 μm). All three aerosol types are assumed as internal mixtures of various components with known SW and LW refractive

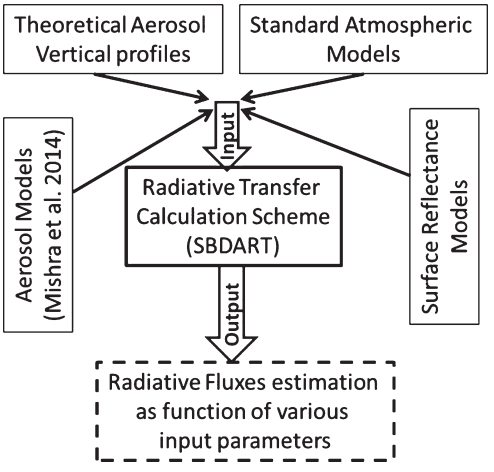

Fig. 2. Layout of the methodology used in this study.

http://dx.doi.org/10.1016/j.heliyon.2015.e00036

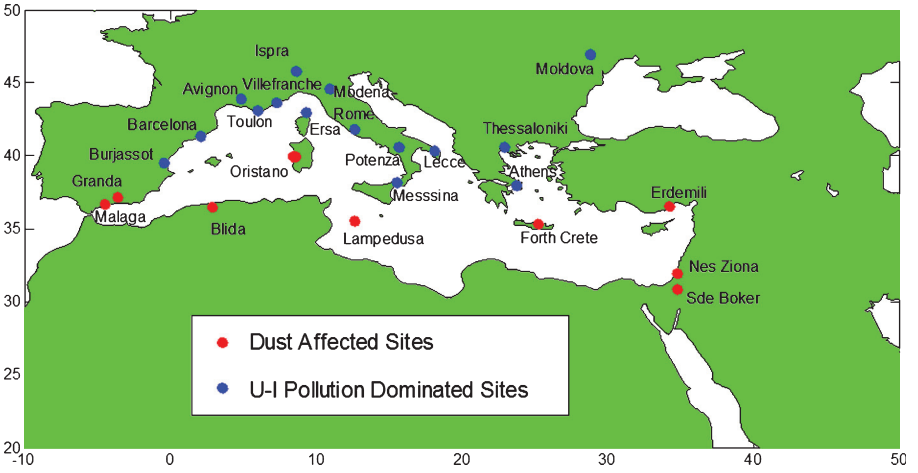

Fig. 3. Locations and names of AERONET sites used in synthesis of aerosol models in this study. Red circles are used for dust affected sites and blue circles are used for urban-industrial (U-I) pollution dominated sites. More details can be found in Mishra et al. (2014).

indices following volume averaged refractive index mixing rule. The assumed components are 'mineral dust + water' for dust; 'mineral dust + black carbon + water' for polluted dust; and 'ammonium sulphate + black carbon + water' for pollution aerosol. The volume fractions are selected such that the refractive indices of the mixture in the 0.4–1.0 μm wavelength range agree with the observed AERONET values. The obtained mean volume fractions are as follows: dust (79.6% mineral dust + 20.4% water); polluted dust (60% mineral dust + 0.5% black carbon + 39.5% water); pollution (38.5% ammonium sulfate + 1.7% black carbon + 59.8% water). We compute (Mie calculation) the aerosol optical properties using these volume fractions combined with the known refractive indices of the components and the observed particle size distributions. Complete details about the classification of AERONET sites, and composition and synthesis process of the aerosol models can be found in Mishra et al. (2014) and references therein (methodology section). Fig. 4 represents the wavelength dependence of the normalized aerosol optical depth (AOD), single scattering albedo (SSA), and the asymmetry parameter (g) for dust, polluted dust, and pollution aerosols. In order to distinguish among various processes associated with aerosol absorption and scattering, we used an additional theoretical non-absorbing/pure scattering aerosol model with similar properties as of dust aerosols, except SSA = 1.0 for all wavelengths.

A homogeneous, 500 m thick aerosol layer at 20 different aerosol layer heights (ALH) from the surface to 10 km altitude is used to explore the effect of the aerosol vertical profiles. To explain the physical processes associated with ALH variation, we have used ALH = 0.5 km for boundary layer aerosol and ALH = 10 km for upper tropospheric layer aerosol (tropical tropopause layer height ≈ 13–18 km) as two extremes in the present study. The aerosol optical

http://dx.doi.org/10.1016/j.heliyon.2015.e00036

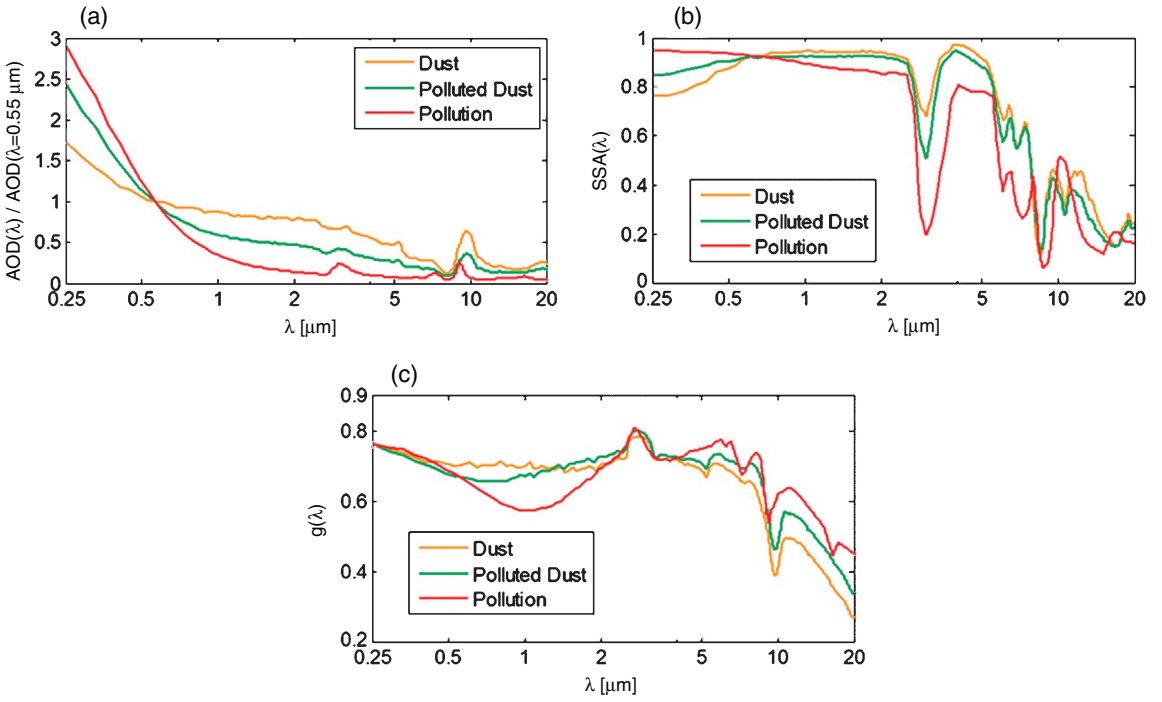

Fig. 4. Wavelength-dependency of the optical properties of various aerosol types (Dust, Polluted Dust and Pollution) (a) aerosol optical depth (AOD) normalized at 0.55 μm, (b) single scattering albedo (SSA), and (c) asymmetry factor (ASYM). Data is adopted from Mishra et al. (2014).

depth (AOD), single scattering albedo (SSA), and asymmetry parameter (g) were kept the same for all ALHs. The two different standard atmospheric models (McClatchey et al., 1972), 'Midlatitude Summer' and 'Midlatitude Winter' are used in this study. The vertical profiles of important atmospheric parameters for these models are provided in Fig. 5. The Midlatitude summer is characterized by significantly higher water vapor density in the lower atmosphere (<5 km) as compared with the Midlatitude winter atmosphere (Fig. 5a). Three different surface reflective properties [Sea water (Tanré et al., 1990), Vegetation (Reeves et al., 1975) and Desert (Staetter and Schroeder, 1978)] are used for surface albedo characterization. The results are shown for the dust aerosol model with the Midlatitude summer atmospheric model over the sea water surface unless specifically mentioned in the figure captions.

The simulations of the clear sky radiative fluxes as a function of various input parameters are done using the SBDART radiative transfer code (Ricchiazzi et al., 1998). SBDART uses the discrete ordinates radiative transfer (DISORT) method to solve the radiative transfer equations (Stamnes et al., 1988). It provides a numerically stable algorithm to solve the equations of a plane-parallel radiative transfer in a vertically inhomogeneous atmosphere. The algorithm calculates the radiation fluxes in a line-by-line manner for each wavelength region. The spectral

http://dx.doi.org/10.1016/j.heliyon.2015.e00036

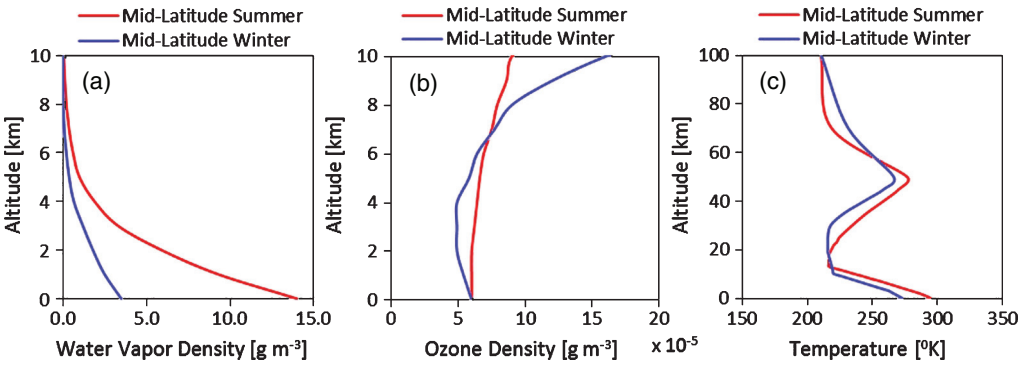

Fig. 5. Vertical profiles of important atmospheric parameters; (a) water vapor density [g m^{-3}] (b) ozone density [g m^{-3}], and (c) temperature [K] for the Mid-Latitude Summer (red) and Mid-Latitude Winter (blue) atmospheric models. Water vapor and ozone density profiles are shown up to 10 km and temperature profiles are shown up to 100 km.

resolution of SBDART run has been fixed to 0.005 μm in the shortwave (SW: 0.25–4.0 μm) and 0.2 μm in the longwave (LW: 4.0–20.0 μm) region which are the standard resolutions provided by this code and sufficient to capture the fine spectral absorption bands for our purpose (Ricchiazzi et al., 1998). The instantaneous clear-sky ARE is calculated as the difference in radiative fluxes perturbation, with and without aerosols at the top of the atmosphere (TOA) and at the surface (SRF) at 60° solar zenith angle (SZA). SZA = 60° is treated as approximate day-time-mean SZA (Coakley and Chylek, 1975) in terms of radiation received at TOA.

In a view of spectral variation of absorption and scattering properties of the atmospheric aerosols and gases with respect to atmospheric windows (explained in Section 1.2), we divide the complete solar and thermal spectral region into three main bands. The specific terminology used for these bands are UV (0.32–0.42 μm), VIS-NIR (0.42–4.0 μm) and TH-IR (4.0–20.0 μm). The separate analysis in these three bands would enable us to follow the dominating processes in each region and would explain the synergism and competition between them.

3. Results and discussion

3.1. Effect of aerosol layer height on the radiation budget and the associated processes

Fig. 6a presents the spectral variation of the aerosol radiative effect (ARE) at TOA for dust aerosols as a function aerosol layer height (ALH) in the UV region. As the aerosol layer height varies from the boundary layer to the upper troposphere, ARE shows a monotonic increase in the 0.32–0.42 μm region. UV radiation <0.32 μm is almost completely absorbed by stratospheric ozone and

http://dx.doi.org/10.1016/j.heliyon.2015.e00036

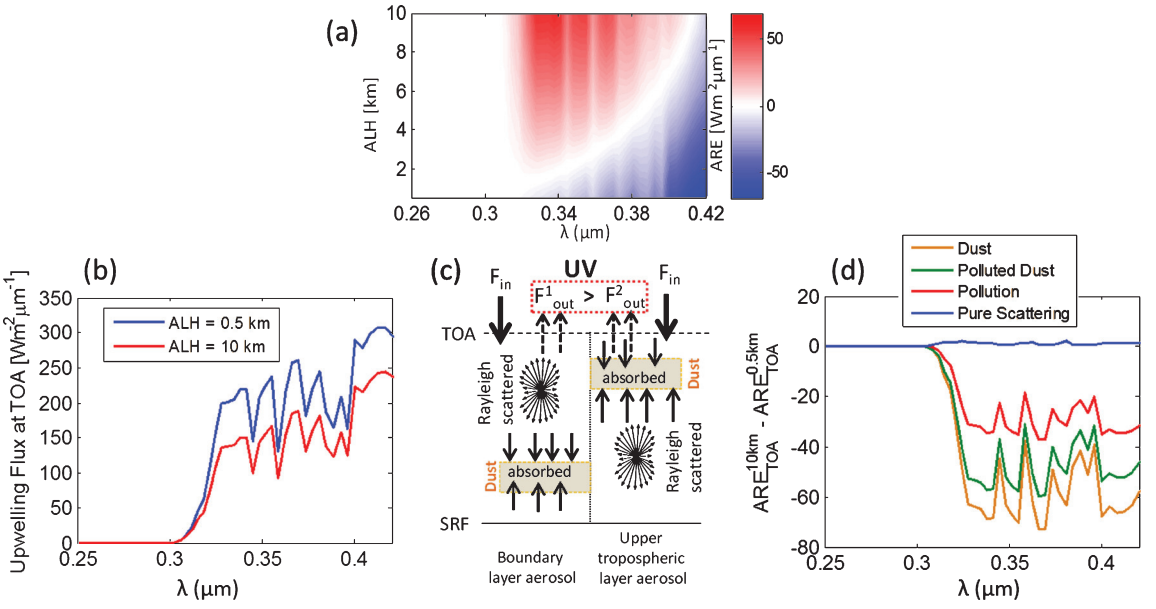

Fig. 6. The spectral variation of (a) the aerosol radiative effect (ARE) for dust aerosol at top of the atmosphere (TOA) [W m^{-2} μm^{-1}] with respect to variations of the aerosol layer height [km], and (b) the upwelling flux at TOA [W m^{-2} μm^{-1}] for two different aerosol layer heights [ALH = 0.5 km and ALH = 10 km] in the UV region. (c) Schematic illustration showing decreased upwelling flux at TOA for an upper tropospheric dust layer (F^2_{out}) as compared to that for a boundary dust layer (F^1_{out}) due to greater availability of upward fraction of Rayleigh scattered radiation for dust absorption in the UV region. F_{in} is incoming radiation at TOA. (d) Spectral variation of difference between estimated ARE at two different cases of aerosol layer height [ALH = 10 km and ALH = 0.5 km] for various aerosol types. The simulations have been done for AOD = 1.0 at 0.55 μm over the sea.

hence ARE did not show any variation in this range. Fig. 6b shows the spectral variation of the upwelling flux at TOA [W m^{-2} μm^{-1}] for dust aerosol for two different aerosol layer heights (boundary layer and upper tropospheric layer aerosol) in the UV region. The simulations have been done for AOD = 1.0 at 0.55 μm over the sea. It shows a substantial decrease in the backscattered radiance at TOA for an upper tropospheric aerosol layer relative to a boundary aerosol layer. Since the aerosols have strong forward scattering ($g > 0.5$), pure scattering aerosols do not alter significantly the background radiation generated by molecular/Rayleigh scattering (N_2 and O_2). However, absorbing aerosols (dust) strongly absorb the molecular scattered radiation and significantly alter the backscattered radiance at TOA (Torres et al., 1998). Since absorbing aerosols at higher altitudes will intercept the more upward fraction of molecular scattered radiation, the backscattered radiance at TOA decreases as compared to that lower altitude aerosol layer. The schematic illustration of the dominant process in the UV region is shown in Fig. 6c. The lower upwelling radiation fluxes at TOA for higher ALH is attributed to higher fraction of upwelling scattered background radiation available for aerosol absorption in the UV

http://dx.doi.org/10.1016/j.heliyon.2015.e00036

region. The robustness of this process for the effect of altitude on ARE can be seen in Fig. 6d. It shows the difference between ARE for two different ALH cases (ALH = 10 & ALH = 0.5 km) for four different aerosol types (dust, polluted dust, pollution and purely scattering aerosols) as a function of wavelength in the UV region. The maximum difference is found for absorbing dust aerosol, where purely scattering aerosols show the negligible difference. These results clearly highlight the importance of absorption characteristic of aerosols to explain the ALH effect on radiation budget in the UV region.

Fig. 7a presents the spectral variation of the ARE_{TOA} for dust aerosols as a function aerosol layer height in the VIS-NIR region. The effect of aerosol layer height on ARE_{TOA} shows high spectral variability. Generally, there is a decrease in ARE with ALH in the VIS-NIR. As opposed to the UV, VIS-NIR includes the solar atmospheric window (~0.4–0.9 μm) with few separated strong gaseous absorption bands (>0.9 μm). The spectral shape of these atmospheric absorption bands (Fig. 1, lower panel) in the VIS-NIR region can be seen as analogues to the ARE variability due to ALH in Fig. 7a. Fig. 7b shows the substantial increase in the upwelling flux at TOA especially in the separated continuous bands (0.6–2.5 μm) for an upper tropospheric aerosol layer relative to that for a boundary

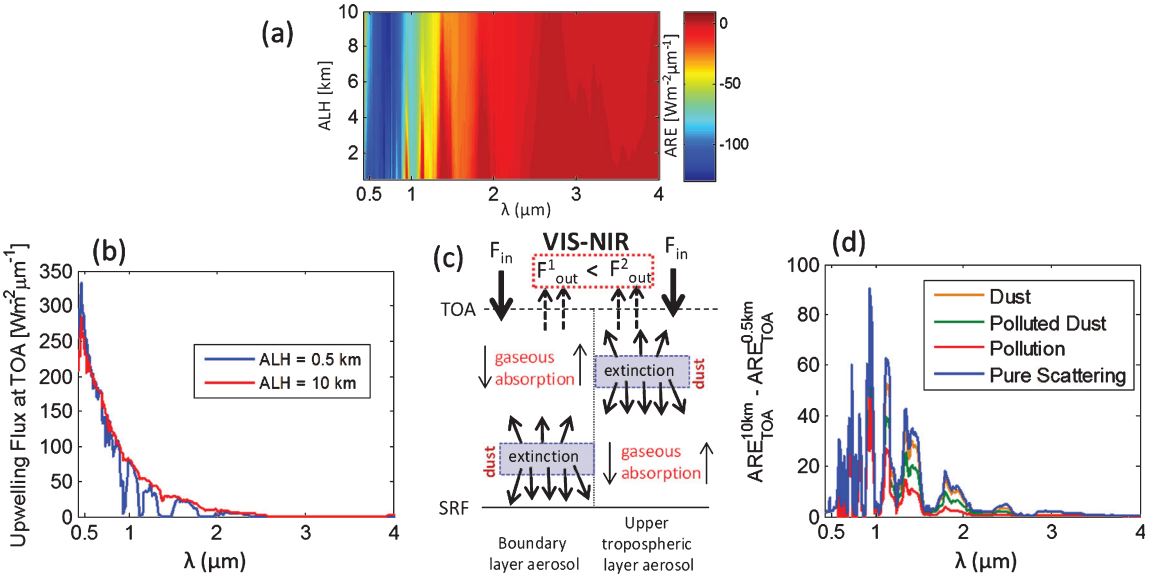

Fig. 7. The spectral variation of (a) the aerosol radiative effect (ARE) for dust aerosol at top of the atmosphere (TOA) [W m^{-2} μm^{-1}] with respect to variations of the aerosol layer height [km], and (b) the upwelling flux at TOA [W m^{-2} μm^{-1}] for two different aerosol layer heights [ALH = 0.5 km and ALH = 10 km] in the VIS-NIR region. (c) Schematic illustration showing increased upwelling flux at TOA for an upper tropospheric dust layer (F^2_{out}) as compared to that for a boundary dust layer (F^1_{out}) due to lesser availability of radiation (direct and scattered) for gaseous absorption in VIS-NIR region. F_{in} is incoming radiation at TOA. (d) Spectral variation of difference between estimated ARE at two different cases of aerosol layer height [ALH = 10 km and ALH = 0.5 km] for various aerosol types. The simulations have been done for AOD = 1.0 at 0.55 μm over the sea.

http://dx.doi.org/10.1016/j.heliyon.2015.e00036

aerosol layer. Since the molecular scattering strength significantly decreases for $\lambda > 0.9$ μm, the significant changes in upwelling flux could be attributed to the interaction between aerosol extinction and the atmospheric absorption.

Fig. 7c shows schematically the dominant process responsible for the increase in the upwelling flux in the VIS-NIR. In cases where the ALH is at low altitude, there is more absorption of the incoming radiation by the atmosphere before reaching the aerosol layer and also with backscattered radiation by aerosols. This process enhances the atmospheric absorption in the specific bands. However, for higher ALH, most of the radiation first interacts with the aerosol layer and, therefore, higher fraction of the incoming radiation is backscattered (depending on aerosol SSA) to the TOA before it can be absorbed in the troposphere. The scattering/absorption effects of the aerosols along with atmospheric gaseous absorption in the VIS-IR are shown in Fig. 7d. The maximum difference is found for pure scattering aerosols followed by dust, polluted dust and pollution. Therefore, we can conclude that absorption by atmospheric gases plays an important role in the variation of ARE_{TOA} with aerosol layer height in the VIS-NIR region.

Fig. 8a shows the spectral variation of the ARE_{TOA} as a function aerosol layer height in the TH-IR region. Similar to the UV region, there is also an increase in ARE with ALH in the TH-IR that is mainly featured in the thermal window (8–13 μm). Fig. 8b shows the substantial decrease in the upwelling flux at TOA in the thermal window region for higher tropospheric aerosol layer relative to boundary aerosol layer. Fig. 8c illustrates the dominant process by a schematic sketch in TH-IR. As aerosols are in thermal balance with their environment, higher ALH will have a lower temperature ($T_2 < T_1$) and, therefore, a decrease in upwelling fluxes at TOA is expected. In general, large aerosol particles show similar radiative behavior as seen for clouds (Koren et al., 2010; Zhou and Savijärvi, 2014) i.e. higher clouds have lower emission of IR radiation. However, there is also gaseous absorption in the thermal region, which can be seen in Fig. 1 (lower panel). Since the source of the thermal radiation is from below the atmosphere as compared with the solar radiation, the gaseous absorption could also assist the aerosol absorption/emission process, which could be seen in 17–20 μm regions. The effect of the size distribution of particles could be seen in TH-IR region (Fig. 8d), where dust shows maximum difference followed by polluted dust and pollution aerosols. Even though the pure scattering aerosols have no absorption at all, but still shows some differences in ARE at different ALH indicates the role of atmospheric absorption in the TH-IR region.

The role of the atmospheric gaseous absorption in the estimation of ARE is shown in Fig. 9, which represents SW (0.25–4 μm)-ARE at TOA as a function

http://dx.doi.org/10.1016/j.heliyon.2015.e00036

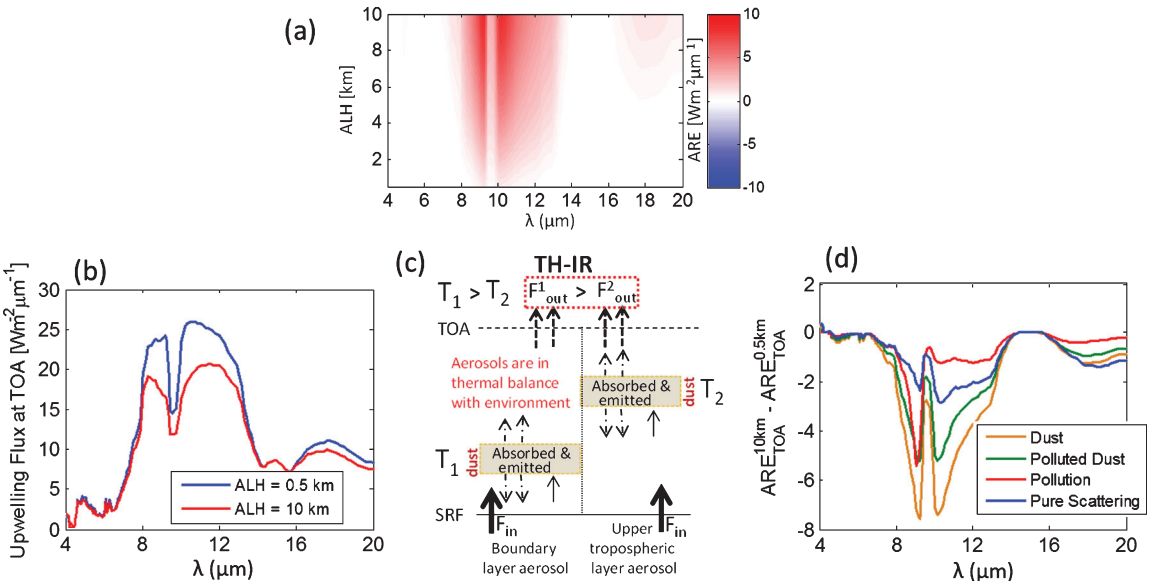

Fig. 8. The spectral variation of (a) the aerosol radiative effect (ARE) for dust aerosol at top of the atmosphere (TOA) [W m^{-2} μm^{-1}] with respect to variations of the aerosol layer height [km], and (b) the upwelling flux at TOA [W m^{-2} μm^{-1}] for two different aerosol layer heights [ALH = 0.5 km and ALH = 10 km] in the TH-IR region. (c) Schematic illustration showing the decreased upwelling flux at TOA for upper tropospheric dust layer (F^2_{out}) as compared to boundary dust layer (F^1_{out}) due to reduction in dust layer-emitted IR in TH-IR region. F_{in} is emitted radiation from Earth's surface. (d) Spectral variation of difference between estimated ARE for ALH = 10 km and ALH = 0.5 km for various aerosol types (Dust, Polluted Dust, Pollution and Pure Scattering aerosols) in TH-IR region. The simulations have been done for AOD = 1.0 at 0.55 μm over the sea.

of ALH and aerosol optical depth (AOD_{550}) for the dust model in two different atmospheric conditions (a) Midlatitude summer and (b) Midlatitude winter. Fig. 9c shows SW-ARE vs. ALH for two AOD cases (τ = 1 and τ = 2) and for two different atmospheric models. Quantitatively, during the summer there is less cooling at TOA as compared with the winter for all AOD ranges. These differences are driven mostly by differences in the water vapor concentrations. In the summer the water vapor loading is higher as compared the winter (Fig. 5a), and hence more radiation in the SW is absorbed which leads to less cooling at TOA. Moreover, Fig. 9c shows that there are significant differences in ARE for two different atmospheric models for the same aerosol model at lower ALH. However, as ALH increase both curves converge and nearly meet at ALH = 10 km. In other words, if the ALH is as high as 10 km, irrespective of atmospheric composition, the estimated ARE will be similar. It shows that (among other atmospheric constituents) the uncertainties in water vapor profiles may significantly affect the estimated ARE and highlights the need of the accuracy in the atmospheric profile of water vapor.

http://dx.doi.org/10.1016/j.heliyon.2015.e00036

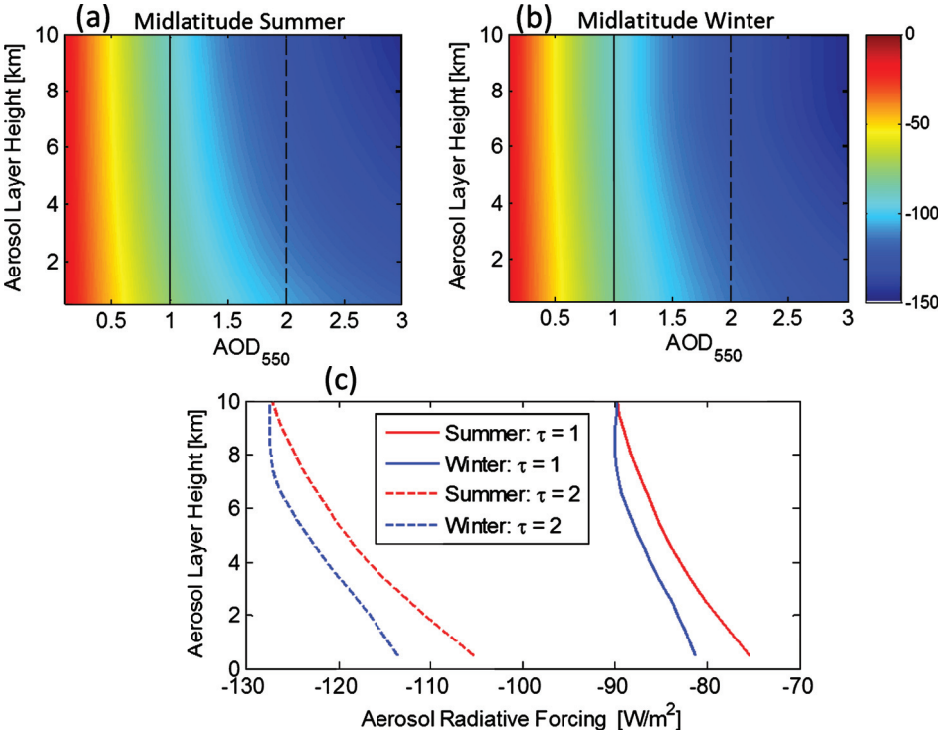

Fig. 9. SW (0.25–4 μm) Aerosol radiative effect (ARE) at TOA [W m^{-2}] as a function of aerosol layer height (ALH) and AOD_{550} for dust model in two different atmospheric conditions (a)Midlatitude summer and (b) Midlatitude winter. (c) SW-ARE vs. ALH for two AOD cases ($\tau = 1$ and $\tau = 2$) and for two different atmospheric models. The simulations have been done over the Sea water surface.

3.2. Sensitivity to AOD, aerosol types and the underlying surface types

To explore the sensitivity to variations of AOD on the effect of aerosol layer height on ARE_{TOA}, the percentage change in ARE_{TOA} is calculated at each aerosol layer relative to that for boundary aerosol layer. The left panels of Fig. 10 shows the entire matrix of ARE_{TOA} variation as a function of ALH and AOD and the right panels show the percentage change in ARE_{TOA} vs. ALH for different AOD cases for all three main regimes. The integrated UV-ARE_{TOA} shows a monotonic increase with ALH within a narrow range of −4 to +4 Wm^{-2} for all AOD cases (Fig. 10a). It shows a transition for ALH around 4–5 km where the UV-ARE_{TOA} changes its sign from negative to positive. This UV-ARE_{TOA} transition from negative to positive could be again explained by re-distribution of upward fraction of backscatter radiation as a function of absorbing aerosol altitude (Section 3.1). The decrease in the ARE with ALH elevation (Fig. 10b) is highlight in the VIS-NIR whereas, it increase with ALH in the TH-IR region (Fig. 10c).

The sensitivity of aerosol layer height to ARE_{TOA} is evident in all three wavelength regimes, with maximum sensitivity in the TH-IR region followed by

http://dx.doi.org/10.1016/j.heliyon.2015.e00036

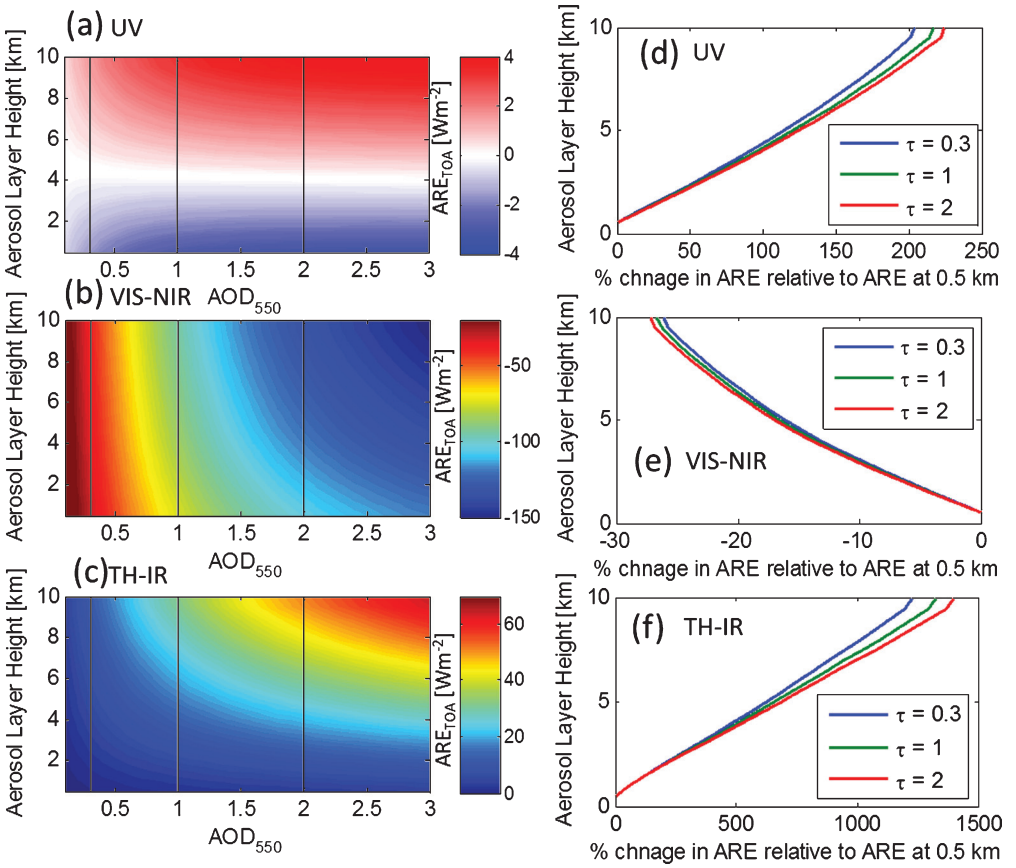

Fig. 10. Aerosol radiative effect (ARE) at TOA [W m^{-2}] as a function of aerosol layer height and AOD_{550} for dust model in the (a) UV, (b) VIS-NIR and (c) TH-IR. The vertical black lines (from left to right) represent the variation for $\tau = 0.3$, $\tau = 1$ and $\tau = 2$, respectively. Percentage (%) change in ARE at TOA relative to ARE at TOA when ALH is 0.5 km as a function of aerosol layer height (ALH) for three different AOD cases ($\tau = 0.3$, $\tau = 1$ and $\tau = 2$) in (d) UV, (e) VIS-NIR and (f) TH-IR region.

the UV and VIS-NIR. Fig. 10d–e shows that there are around 120%, 20% and 2.5% change (lower bound) in ARE_{TOA} for per unit km change in ALH in the TH-IR, UV and VIS-NIR region, respectively. The sensitivity to AOD shows its effectiveness even at lower AOD cases ($\tau = 0.3$). However, the differences between lower and higher AOD cases grow within a narrow range with ALH elevation. Our results suggest that the effect of ALH on ARE_{TOA} is very significant even in low aerosol loading.

Fig. 11 shows ARE_{TOA} vs. ALH for various aerosol types in all three wavelength region for unit AOD. Dust shows maximum gradient for ARE_{TOA} change with ALH in all three regimes followed by polluted dust and pollution. This observation could be explained by changing spectral SSA behavior of aerosol types in 0.25–20 μm range (Fig. 4). Aerosol absorption along with molecular scattering are primarily responsible for the changes in ARE in the UV

http://dx.doi.org/10.1016/j.heliyon.2015.e00036

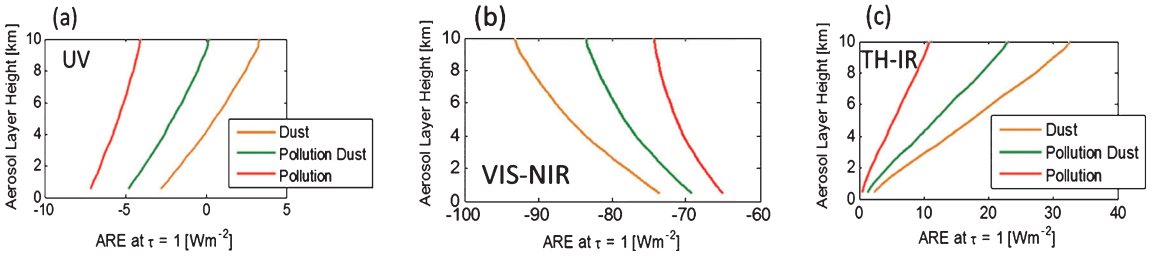

Fig. 11. Aerosol radiative effect (ARE) at TOA [W m^{-2}] as a function of aerosol layer height for different aerosol types (dust, polluted dust, pollution) in (a) UV, (b) VIS-NIR and (c) TH-IR region. The simulations have been done for AOD = 1.0 at 0.55 μm over the Sea water surface.

region whereas, aerosol scattering coupled with atmospheric absorption are the key processes in the VIS-NIR, and size of particles with their absorption properties are important in the TH-IR region (Section 4.1). Fig. 4 evidently present that dust have maximum absorption in UV and become more scatter in VIS-NIR region as compared with other two aerosol types. This type of spectral behavior of SSA is also true for most of the dust particles across the globe (Hess et al., 1998). This observation indicates the important role of absorption/scattering and microphysical properties of aerosols in influencing the effect of aerosol vertical distribution on ARE_{TOA}.

Fig. 12 shows the percentage change in dust-ARE_{TOA} (relative to ARE_{TOA} when ALH is 0.5 km) as a function of aerosol layer height (ALH) for three different surfaces (Sea water, Vegetation and Desert) in the (a) UV (b) VIS-NIR and (c) TH-IR region. Relatively high absorbing underlying surfaces (e.g. Sea water, vegetation) shows maximum sensitivity to ARE_{TOA} change with ALH as compared to relatively bright surfaces (e.g. Desert) in the UV region (Fig. 12a). Torres et al. (1998) have explained that the importance of molecular scattering reduced for bright surfaces below the aerosol layer in the UV region, thereby the altitude dependence of aerosol absorption reduced too.

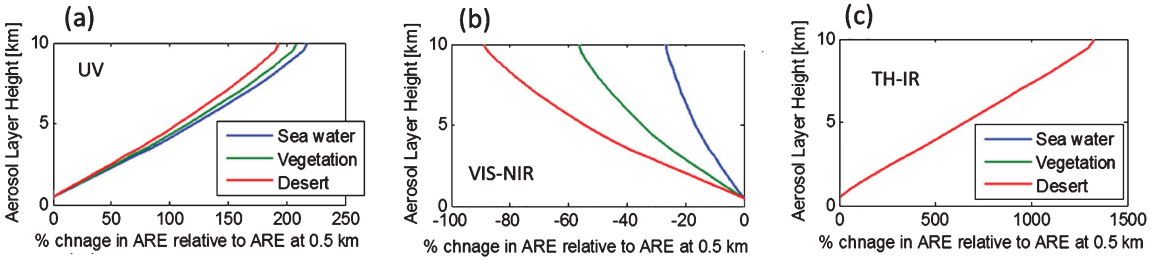

Fig. 12. Percentage (%) change in dust-ARE at TOA relative to ARE at TOA when ALH is 0.5 km as a function of aerosol layer height (ALH) for three different surfaces (Sea water, Vegetation and Desert) in (a) UV, (b) VIS-NIR and (c) TH-IR region. The results have shown for AOD = 1.0 at 0.55 μm.

http://dx.doi.org/10.1016/j.heliyon.2015.e00036

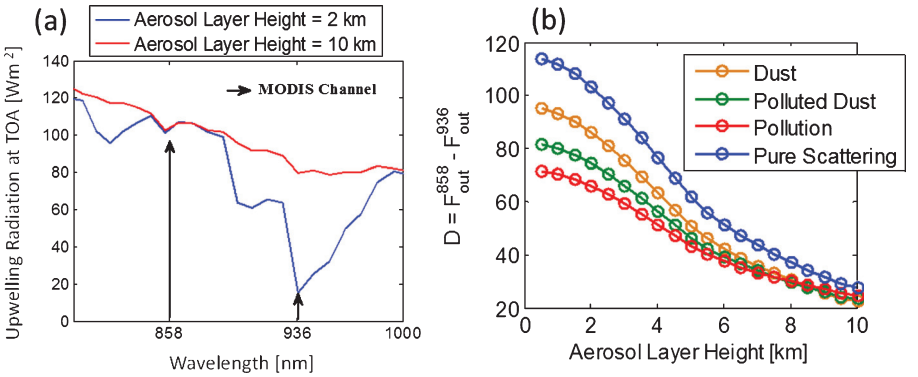

Fig. 13. (a) Upwelling radiation flux at TOA (dust) for two different aerosol layer height (ALH = 2 km and ALH = 10 km) in NIR region, black arrows showing MODIS channels availability in this wavelength region. (b) Difference (D) between upwelling radiation flux at TOA between 858 nm and 936 nm as a function of ALH for various aerosol types.

In the VIS-NIR region, bright surfaces show maximum sensitivity as compared to dark surfaces (Fig. 12b). For bright underlying surface below the aerosol layer, the multiple scattering between surface and aerosol layer increases the probability of interaction of radiation with atmospheric gases and therefore enhance the atmospheric absorption. However, in the TH-IR region, as expected surface reflectivity is not indicative of emissivity and therefore did not show any sensitivity to change in ARE_{TOA} with respect to aerosol layer height (Fig. 12c).

4. Conclusion

We studied the effect of the aerosol vertical distributions on the ARE using the SBDART radiative transfer model. The underlying physical processes associated with the effect of aerosol layer height on the ARE have been explored using four aerosol models (dust, polluted dust, pollution and pure scattering aerosols). We have used a 500 m thick homogeneous aerosol layer at 20 different ALH from 0 to 10 km altitudes as different aerosol vertical profiles in this study. The estimated ARE strongly depends on the ALH for the different spectral regimes. The dominant physical processes for the different spectral regimes are: (1) In the UV region, due to increase in upwelling fraction of molecular scattered radiation for high altitude aerosol layers, aerosol absorption is enhanced significantly and modulates the ARE_{TOA} variability with ALH. (2) In the VIS-NIR region, atmospheric gaseous absorption plays an important role in the variation of ARE_{TOA} with ALH, which also depends on the scattering/absorbing nature of the aerosols. (3) In the TH-IR region, the size distributions of the particles and their absorption properties modulate the absorption and emission of thermal radiation. The analyses for various aerosol types strengthened the robustness of explained mechanisms.

http://dx.doi.org/10.1016/j.heliyon.2015.e00036

The various sensitivity analyses on the effect of ALH on ARE highlight the parameters responsible for the variations discussed in this study. The change in ARE with changing aerosol layer height shows significant sensitivity in the TH-IR region, followed by the UV and VIS-NIR. These changes are evident even in low aerosol loading cases. The maximum sensitivity to altitude is found for dust, followed by polluted dust and pollution in all three different wavelength regions. This result is explained by the relative strength of the spectral absorption/scattering properties of the different aerosol types. The sensitivities of surface reflectivity are also significant in the VIS-NIR and UV regions whereas it is insensitive in the TH-IR region. Our results indicate that errors in the water vapor profiles lead to substantial uncertainties in the ARE estimation.

The spectral signatures of aerosols and how they change with their vertical distributions in the UV and thermal regions has received much attention recently and frequently used in estimation of aerosol layer heights (DeSouza-Machado et al., 2015; DeSouza-Machado et al., 2010; Han and Sohn, 2013; Torres et al., 2013; Torres et al., 1998). Recently DeSouza-Machado et al. (2015) reported a novel methodology to determine the height of atmospheric dust and ash plumes through synergy of Atmospheric Infrared Sounder (AIRS)-inferred thermal infrared radiance and the Moderate Imaging Spectroradiometer (MODIS)-derive visible aerosol optical depth. They have selectively used the spectral signature of dust and volcanic ash in 9–12 μm for varying altitudes and it's relation with visible AOD. Similarly, Torres et al. (2013; 1998) used the UV spectral behavior of absorbing aerosols to estimate their heights and other optical properties in this wavelength region.

Our study highlights the ALH effect on the aerosol radiance at TOA in the NIR region. Fig. 13a shows the NIR upwelling radiation flux at TOA (dust) for two different aerosol layer heights (ALH = 2 km and ALH = 10 km). The variation of ALH has no effect on the outgoing radiation at 858 nm (shown by a black arrow) but has a significant effect at 936 nm. These two channels (858 nm and 936 nm) are available in MODIS observations and used for estimating the aerosol properties and the water vapor content, respectively. The absorption of water vapor at 936 nm (NIR) is well known and widely used for estimation of the water vapor amount from remote sensing measurements (Gao and Kaufman, 2003; Kaufman and Gao, 1992). The change in the spectral signature of aerosol radiance due to ALH variation (Fig. 13a) gives an opportunity to see the sensitivity of the difference between these two channels against ALH. Fig. 13b shows the difference between the upwelling radiation at 858 nm and 936 nm as a function of ALH for four different aerosol types. It shows that the difference in outgoing radiance at these two wavelengths has a strong sensitivity to ALH for all aerosol types. Purely scattering aerosol shows maximum sensitivity and it decreases for more absorbing aerosols in this wavelength region. These results

http://dx.doi.org/10.1016/j.heliyon.2015.e00036

clearly manifest the role of water vapor absorption with aerosol layer height variation. In the clear sky conditions, the synergy between the radiance information from these MODIS channels and the known atmospheric water vapor profiles (retrieved from AIRS) could be used for estimating the aerosol layer height on the global scale. These results can also serve as the basis for further studies on accurate estimation of water vapor profiles using known aerosol vertical distribution from ground-based and satellite-borne active remote sensors like Micro-Pulse Lidar Network, MPLNET (Welton et al., 2006) and Cloud-Aerosol Lidar and Infrared Pathfinder Satellite Observations, CALIPSO (Winker et al., 2003), respectively.

Declarations

Author contribution statement

Amit K. Mishra: Conceived and designed the experiments; Performed the experiments; Analyzed and interpreted the data; Wrote the paper.

Ilan Koren: Conceived and designed the experiments; Analyzed and interpreted the data; Contributed reagents, materials, analysis tools or data.

Yinon Rudich: Conceived and designed the experiments.

Funding statement

This work was supported by German Israeli Science Foundation (GIF) (1136-26.8/2011).

Competing interest statement

The authors declare no conflict of interest.

Additional information

No additional information is available for this paper.

Acknowledgements

YR acknowledges support from the Dollond Charitable Trust.

References

Altaratz, O., Koren, I., Remer, L., Hirsch, E., 2014. Review: Cloud invigoration by aerosols—Coupling between microphysics and dynamics. Atmos. Res. 140, 38–60.

Baker, M.B., Peter, T., 2008. Small-scale cloud processes and climate. Nature 451, 299–300.

http://dx.doi.org/10.1016/j.heliyon.2015.e00036

Benedetti, A., Morcrette, J.J., Boucher, O., Dethof, A., Engelen, R., Fisher, M., et al., 2009. Aerosol analysis and forecast in the European centre for medium-range weather forecasts integrated forecast system: 2. Data assimilation. J. Geophys. Res.: Atmos. (1984–2012) 114, D13205.

Bergstrom, R., Schmidt, K., Coddington, O., Pilewskie, P., Guan, H., Livingston, J., et al., 2010. Aerosol spectral absorption in the Mexico City area: results from airborne measurements during MILAGRO/INTEX B. Atmos. Chem. Phys. 10, 6333–6343.

Bond, T.C., Doherty, S.J., Fahey, D., Forster, P., Berntsen, T., DeAngelo, B., et al., 2013. Bounding the role of black carbon in the climate system: A scientific assessment. J. Geophys. Res: Atmos. 118, 5380–5552.

Boucher, O., Randall, D., Artaxo, P., Bretherton, C., Feingold, G., Forster, P., et al., 2013. Clouds and Aerosols. In: Stocker, T.F., Qin, D., Plattner, G.-K., Tignor, M., Allen, S.K., Boschung, J., et al. (Eds.), Climate Change 2013: The Physical Science Basis Contribution of Working Group I to the Fifth Assessment Report of the Intergovernmental Panel on Climate Change. Cambridge University Press, Cambridge, United Kingdom and New York, NY, USA.

Carslaw, K., Boucher, O., Spracklen, D., Mann, G., Rae, J., Woodward, S., et al., 2010. A review of natural aerosol interactions and feedbacks within the Earth system. Atmos. Chem. Phys. 10, 1701–1737.

Chand, D., Wood, R., Anderson, T., Satheesh, S., Charlson, R., 2009. Satellite-derived direct radiative effect of aerosols dependent on cloud cover. Nat. Geosci. 2, 181–184.

Choi, J.-O., Chung, C.E., 2014. Sensitivity of aerosol direct radiative forcing to aerosol vertical profile. Tellus B 66, 24376.

Christopher, S.A., Johnson, B., Jones, T.A., Haywood, J., 2009. Vertical and spatial distribution of dust from aircraft and satellite measurements during the GERBILS field campaign. Geophys. Res. Lett. 36, L06806.

Coakley Jr., J.A., Chylek, P., 1975. The two-stream approximation in radiative transfer: Including the angle of the incident radiation. J. Atmos. Sci. 32, 409–418.

Costantino, L., Bréon, F.-M., 2013. Aerosol indirect effect on warm clouds over South-East Atlantic, from co-located MODIS and CALIPSO observations. Atmos. Chem. Phys. 13, 69–88.

DeSouza-Machado, S., Strow, L., Maddy, E., Torres, O., Thomas, G., Grainger, D., et al., 2015. A novel retrieval of daytime atmospheric dust and

 http://dx.doi.org/10.1016/j.heliyon.2015.e00036

volcanic ash heights through a synergy of AIRS infrared radiances and MODIS L2 optical depths. Atmos. Meas. Tech. Discuss. 8, 443–485.

DeSouza-Machado, S., Strow, L., Imbiriba, B., McCann, K., Hoff, R., Hannon, S., et al., 2010. Infrared retrievals of dust using AIRS: Comparisons of optical depths and heights derived for a North African dust storm to other collocated EOS A-Train and surface observations. J. Geophys. Res.: Atmos. 115, D15201.

Feng, Y., Kotamarthi, V., Coulter, R., Zhao, C., Cadeddu, M., 2015. Radiative and thermodynamic responses to aerosol extinction profiles during the pre-monsoon month over South Asia. Atmos. Chem. Phys. Discuss. 15, 16901–16943.

Gao, B.C., Kaufman, Y.J., 2003. Water vapor retrievals using Moderate Resolution Imaging Spectroradiometer (MODIS) near-infrared channels. J. Geophys. Res.: Atmos. 108, D13, 4389.

Ghan, S.J., Liu, X., Easter, R.C., Zaveri, R., Rasch, P.J., 2012. Yoon J-H, et al. Toward a minimal representation of aerosols in climate models: Comparative decomposition of aerosol direct, semidirect, and indirect radiative forcing. J. Climate 25, 6461–6476.

Graaf, M., Tilstra, L., Wang, P., Stammes, P., 2012. Retrieval of the aerosol direct radiative effect over clouds from spaceborne spectrometry. J. Geophys. Res.: Atmos. (1984–2012) 117, D07207.

Han, H.J., Sohn, B., 2013. Retrieving Asian dust AOT and height from hyperspectral sounder measurements: An artificial neural network approach. J. Geophys. Res: Atmos. 118, 837–845.

Hansell, R., Tsay, S., Ji, Q., Hsu, N., Jeong, M., Wang, S., et al., 2010. An assessment of the surface longwave direct radiative effect of airborne Saharan dust during the NAMMA field campaign. J. Atmos. Sci. 67, 1048–1065.

Haywood, J., Shine, K., 1997. Multispectral calculations of the direct radiative forcing of tropospheric sulphate and soot aerosols using a column model. Q. J. Roy. Meteorol. Soc. 123, 1907–1930.

Heintzenberg, J., Hermann, M., Weigelt, A., Clarke, A., Kapustin, V., Anderson, B., et al., 2011. Nearglobal aerosol mapping in the upper troposphere and lowermost stratosphere with data from the CARIBIC project. Tellus B 63, 875–890.

Hess, M., Koepke, P., Schult, I., 1998. Optical properties of aerosols and clouds: The software package OPAC. B. Am. Meteorol. Soc. 79, 831–844.

 http://dx.doi.org/10.1016/j.heliyon.2015.e00036

Kahn, R.A., 2012. Reducing the uncertainties in direct aerosol radiative forcing. Surv. Geophys. 33, 701–721.

Kaufman, Y.J., Gao, B.-C., 1992. Remote sensing of water vapor in the near IR from EOS/MODIS. IEEE Trans. Geosci. Remote Sens. 30, 871–884.

Keil, A., Haywood, J.M., 2003. Solar radiative forcing by biomass burning aerosol particles during SAFARI 2000: A case study based on measured aerosol and cloud properties. J. Geophys. Res.: Atmos. (1984–2012) 108 (D13), SAF3.1–SAF3.10.

Kinne, S., Schulz, M., Textor, C., Guibert, S., Balkanski, Y., Bauer, S.E., et al., 2006. An AeroCom initial assessment – optical properties in aerosol component modules of global models. Atmos. Chem. Phys. 6, 1815–1834.

Kleidman, R.G., Smirnov, A., Levy, R.C., Mattoo, S., Tanre, D., 2012. Evaluation and wind speed dependence of MODIS aerosol retrievals over open ocean. IEEE Trans. Geosci. Remote Sens. 50, 429–435.

Kokhanovsky, A., Deuzé, J., Diner, D., Dubovik, O., Ducos, F., Emde, C., et al., 2010. The inter-comparison of major satellite aerosol retrieval algorithms using simulated intensity and polarization characteristics of reflected light. Atmos. Meas. Tech. 3, 909–932.

Koren, I., Remer, L., Altaratz, O., Martins, J., Davidi, A., 2010. Aerosol-induced changes of convective cloud anvils produce strong climate warming. Atmos. Chem. Phys. 10, 5001–5010.

Kulmala, M., Asmi, A., Lappalainen, H., Baltensperger, U., Brenguier, J.-L., Facchini, M., et al., 2011. General overview: European Integrated project on Aerosol Cloud Climate and Air Quality interactions (EUCAARI)–integrating aerosol research from nano to global scales. Atmos. Chem. Phys. 11, 13061–13143.

Leibensperger, E.M., Mickley, L.J., Jacob, D.J., Chen, W.T., Seinfeld, J.H., Nenes, A., et al., 2012. Climatic effects of 1950–2050 changes in US anthropogenic aerosols – Part 1: Aerosol trends and radiative forcing. Atmos. Chem. Phys. 12, 3333–3348.

Li, Z., Niu, F., Fan, J., Liu, Y., Rosenfeld, D., Ding, Y., 2011. Long-term impacts of aerosols on the vertical development of clouds and precipitation. Nat. Geosci. 4, 888–894.

Li, Z., Zhao, X., Kahn, R., Mishchenko, M., Remer, L., Lee, K.-H., et al., 2009. Uncertainties in satellite remote sensing of aerosols and impact on monitoring its long-term trend: a review and perspective. Ann. Geophys. 27, 2755–2770.

http://dx.doi.org/10.1016/j.heliyon.2015.e00036

Liao, H., Seinfeld, J., 1998. Radiative forcing by mineral dust aerosols: sensitivity to key variables. J. Geophys. Res.: Atmos. (1984–2012) 103, 31637–31645.

McClatchey, R.A., Fenn, R., Selby, J.A., Volz, F., Garing, J., 1972. Optical properties of the atmosphere. Environmental research papers. DTIC Document. AIR FORCE CAMBRIDGE RESEARCH LABS HANSCOM AFB, MA, pp. 108.

Meyer, K., Platnick, S., Oreopoulos, L., Lee, D., 2013. Estimating the direct radiative effect of absorbing aerosols overlying marine boundary layer clouds in the southeast Atlantic using MODIS and CALIOP. J. Geophys. Res.: Atmos. 118, 4801–4815.

Mishra, A., Klingmueller, K., Fredj, E., Lelieveld, J., Rudich, Y., Koren, I., 2014. Radiative signature of absorbing aerosol over the eastern Mediterranean basin. Atmos. Chem. Phys. 14, 7213–7231.

Myhre, G., Shindell, D., Bréon, F.-M., Collins, W., Fuglestvedt, J., Huang, J., et al., 2013a. Anthropogenic and natural radiative forcing. In: Stocker, F., Qin, D., Plattner, G.-K., Tignor, M., Allen, S.K., Boschung, J., et al. (Eds.), Climate Change 2013: The Physical Science Basis Contribution of Working Group I to the Fifth Assessment Report of the Intergovernmental Panel on Climate Change. Cambridge University Press, Cambridge, United Kingdom and New York, NY, USA.

Myhre, G., Samset, B.H., Schulz, M., Balkanski, Y., Bauer, S., Berntsen, T.K., et al., 2013b. Radiative forcing of the direct aerosol effect from AeroCom Phase II simulations. Atmos. Chem. Phys. 13, 1853–1877.

Paredes-Miranda, G., Arnott, W., Jimenez, J., Aiken, A., Gaffney, J., Marley, N., 2009. Primary and secondary contributions to aerosol light scattering and absorption in Mexico City during the MILAGRO 2006 campaign. Atmos. Chem. Phys. 9, 3721–3730.

Peters, K., Quaas, J., Bellouin, N., 2011. Effects of absorbing aerosols in cloudy skies: a satellite study over the Atlantic Ocean. Atmos. Chem. Phys. 11, 1393–1404.

Raes, F., Liao, H., Chen, W.T., Seinfeld, J.H., 2010. Atmospheric chemistry-climate feedbacks. J. Geophys. Res.: Atmos. 115, D12121.

Reeves, R., Anson, A., Landen, D., 1975. First Ed. Manual of remote sensing. American Society Photogrammetry, 2144 pp.

Ricchiazzi, P., Yang, S., Gautier, C., Sowle, D., 1998. SBDART: A research and teaching software tool for plane-parallel radiative transfer in the Earth's atmosphere. Bull. Am. Meteorol. Soc. 79, 2101–2114.

http://dx.doi.org/10.1016/j.heliyon.2015.e00036

Rosenfeld, D., 2014. Climate effects of aerosol-cloud interactions. Science 1247490 (379), 343.

Schwartz, S.E., 2004. Uncertainty requirements in radiative forcing of climate change. J. Air Waste Manage. Association 54, 1351–1359.

Seinfeld, J.H., Pandis, S.N., 2012. Atmospheric chemistry and physics: from air pollution to climate change, 2nd edition, John Wiley & Sons, New York, pp. 98–137.

Staetter, R., Schroeder, M., 1978. Spectral characteristics of natural surfaces. Proc. Int. Conf. on Earth Observation from Space and Management of Planetary Resources. Toulouse, France, Council of Europe, Commission of the European Communities, and European Association of Remote Sensing Laboratories, 661 pp.

Stamnes, K., Tsay, S.-C., Wiscombe, W., Jayaweera, K., 1988. Numerically stable algorithm for discrete-ordinate-method radiative transfer in multiple scattering and emitting layered media. Appl. Optics 27, 2502–2509.

Stevens, B., Feingold, G., 2009. Untangling aerosol effects on clouds and precipitation in a buffered system. Nature 461, 607–613.

Tanré, D., Bréon, F., Deuzé, J., Dubovik, O., Ducos, F., François, P., et al., 2011. Remote sensing of aerosols by using polarized, directional and spectral measurements within the A-Train: the PARASOL mission. Atmos. Meas. Tech. 4, 1383–1395.

Tanré, D., Deroo, C., Duhaut, P., Herman, M., Morcrette, J., Perbos, J., et al., 1990. Technical note Description of a computer code to simulate the satellite signal in the solar spectrum: the 5S code. Int. J. Remote Sens. 11, 659–668.

Tao, W.K., Chen, J.P., Li, Z., Wang, C., Zhang, C., 2012. Impact of aerosols on convective clouds and precipitation. Rev. Geophys. 50, 2.

Torres, O., Ahn, C., Chen, Z., 2013. Improvements to the OMI near-UV aerosol algorithm using A-train CALIOP and AIRS observations. Atmos. Meas. Tech. 6, 3257–3270.

Torres, O., Bhartia, P., Herman, J., Ahmad, Z., Gleason, J., 1998. Derivation of aerosol properties from satellite measurements of backscattered ultraviolet radiation: Theoretical basis. J. Geophys. Res.: Atmos. (1984–2012) 103, 17099–17110.

van de Hulst, H., 1981. Light Scattering by Small Particles. Dover Publication, New York, pp. 470.

 http://dx.doi.org/10.1016/j.heliyon.2015.e00036

Vuolo, M.R., Schulz, M., Balkanski, Y., Takemura, T., 2014. A new method for evaluating the impact of vertical distribution on aerosol radiative forcing in general circulation models. Atmos. Chem. Phys. 14, 877–897.

Welton, E.J., Campbell, J.R., Berkoff, T.A., Valencia, S., Spinhirne, J.D., Holben, B., et al., 2006. The NASA Micro-Pulse Lidar Network (MPLNET): an overview and recent results. Opt. Pur. Apl 39, 67–74.

Wilcox, E., 2012. Direct and semi-direct radiative forcing of smoke aerosols over clouds. Atmos. Chem. Phys. 12, 139–149.

Winker, D.M., Pelon, J.R., McCormick, M.P., 2003. The CALIPSO mission: Spaceborne lidar for observation of aerosols and clouds. 1, March 24, Proc. SPIE, Lidar Remote Sensing for Industry and Environment Monitoring III, 4893, pp. 1–11.

Zarzycki, C.M., Bond, T.C., 2010. How much can the vertical distribution of black carbon affect its global direct radiative forcing? Geophys. Res. Lett. 37, 20.

Zhang, X., Wang, Y., Niu, T., Zhang, X., Gong, S., Zhang, Y., et al., 2012. Atmospheric aerosol compositions in China: spatial/temporal variability, chemical signature, regional haze distribution and comparisons with global aerosols. Atmos. Chem. Phys. 12, 779–799.

Zhou, Y., Savijärvi, H., 2014. The effect of aerosols on long wave radiation and global warming. Atmos. Res. 135, 102–111.

 http://dx.doi.org/10.1016/j.heliyon.2015.e00036